Chapter 5

Tensile and Compressive Behavior

In the present chapter, the ambient temperature tensile and compressive properties of the AXM520 alloy and NCs have been evaluated. Detailed analyses of the strain-hardening response and fracture surfaces of the tested specimens are carried out. The dislocations in the tested specimens have been characterized using TEM. A summary of the tensile and compressive behavior is presented at the end of this chapter.

5.1 Evaluation of mechanical properties

5.1.1 Tensile Yield Strength, Ultimate Tensile Strength, and % Elongation

Figure 5.1(a) shows the typical engineering stress vs. engineering strain curves obtained at ambient temperature from the AXM520 alloy and the NCs. The tensile properties, i.e., Yield Strength (YS), Ultimate Tensile Strength (UTS), and %Elongation (%El) calculated from Figure 5.1(a) are presented in Figure 5.1(b). The magnitudes of YS, UTS, and %El of the AXM520 alloy were 80.4±8.2 MPa, 111.28±7.1 MPa, and 1.03±0.03%, respectively. All the NCs exhibited superior tensile properties than the AXM520 alloy. The NC with 0.5 (wt.%) SiC_{np} (i.e., NC0.5SiC) exhibited the lowest YS, UTS, and %El among the NCs. The NC2.0SiC exhibited the best tensile properties among the nanocomposites employed in the current study. The YS, UTS, and %El of the NC2.0SiC enhanced by 37.2, 69.8, and 200.9%, respectively, compared to the AXM520 alloy. Unfortunately, with further increase in the nanoparticle's concentration in the nanocomposites, i.e., in the NC3.0SiC, there was a marginal increase in the YS with a deterioration in the UTS and %El compared to the NC1.0SiC and NC2.0SiC. Thus, the YS of the NCs improved gradually with the increase in the SiC_{np} concentration up to 3.0 (wt.%). However, the UTS and %El of the nanocomposite declined with the addition of more than 2.0 (wt.%) SiC_{np} to the AXM520 alloy. Goh et al. [71] too reported an improvement in the YS and UTS of pure Mg with additions of Y_2O_3 nanoparticles up to 2.0 vol.% without deteriorating its ductility much. The low values of %El of the Mg-Al-Ca (AX) and Mg-Al-Ca-Mn (AXM) alloys were also reported previously. The presence of the brittle A12, C36, and C14 phases was responsible for the low elongation of the alloys. Sanyal et al. [35] mentioned that the hardness and modulus mismatch between the matrix and Ca-rich phases introduced a large amount of decohesion in the AXM alloy. The network of Ca-rich phase in their investigation facilitated crack propagation during fracture. Thus, the discontinuous network of

the C36 phase in the NCs significantly inhibited crack propagation, leading to their improved elongation compared to the AXM520 alloy. However, as the concentration of the SiC_{np} increased to 3.0 (wt.%) in the NC3.0SiC, the agglomeration of the nanoparticles increased, resulting in an inferior %El of the NC3.0SiC.

5.1.2 Compressive Yield Strength and Ultimate Compressive Strength

The representative stress-strain plot of the AXM520 alloy, as well as NCs obtained from the uniaxial compressive test at ambient temperature, is shown in Figure 5.1(c). The nature of the plots is in good agreement with the previously reported compressive plots on Mg-based alloys and composites [72,76,78]. The compression properties evaluated from Figure 5.1(c) are presented in Figure 5.1(d). All the NCs exhibited superior compressive strength than the AXM520 alloy. Among the NCs, the NC0.5SiC demonstrated the minimum CYS and UCS. The NC2.0SiC exhibited the best compressive strength among the NCs. The CYS and UCS of the NC2.0SiC enhanced by 23.7 and 53.9% than the AXM520 alloy. Unfortunately, with further increase in the nanoparticles content in the NCs, i.e., in the NC3.0SiC, there is a marginal increase in the CYS with a deterioration in the UCS than the NC2.0SiC. Thus, the CYS of the NCs improved gradually with the increase in the SiC_{np} concentration up to 3.0 (wt.%). However, the UCS declined with the addition of more than 2.0 (wt.%) SiC_{np} to the AXM520 alloy due to the significant agglomeration of the nanoparticles, which weakened the strain-hardening response of the NCs. Accordingly, the UCS value of the NC3.0SiC decreased.

5.1.3 Strain-hardening responses

Hollomon equation [98] relates the true stress (σ) with the true plastic strain (ε) from the point of yielding to UTS through the following equation.

$$\sigma = k\epsilon^n \qquad \text{Equation 5.1}$$

where n and k are the strain-hardening exponent (SHE) and strength coefficient, respectively. The ability of a material to undergo strain-hardening is quantified by the parameter SHE (n). A plot of true stress against true strain in a log-log scale up to UTS results in a straight line. The gradient of the line is SHE (n). Figure 5.2(a) shows the $\log(\sigma_{True})$ vs. $\log(\varepsilon_{true})$ plot for the AXM520 alloy and NCs. The AXM520 alloy exhibits a 'n' value of 0.31, whereas the same

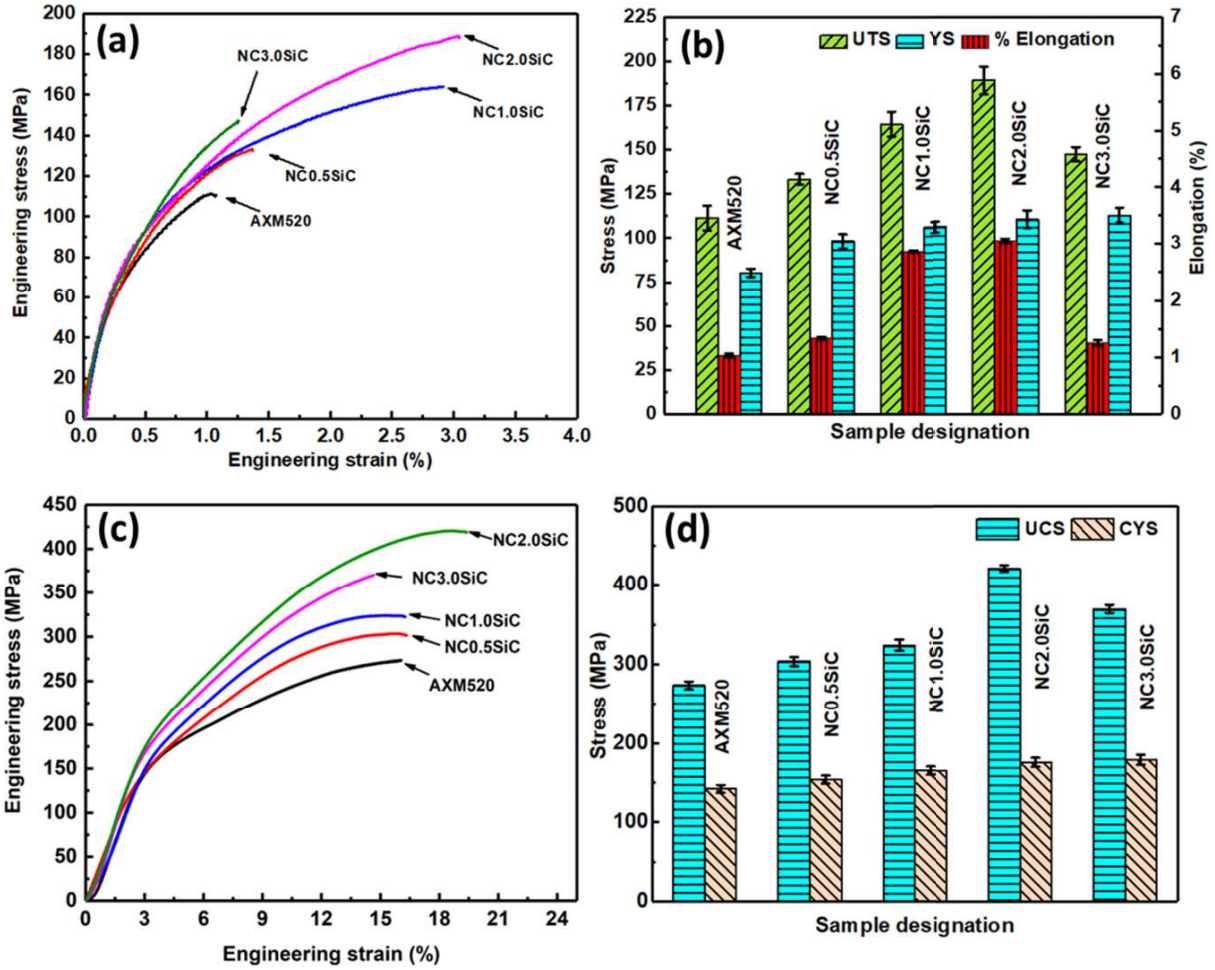

Figure 5.1 (a) Typical engineering stress-strain curves obtained from tensile tests of the AXM520 alloy and NCs, and (b) tensile properties calculated from 'a'; (c) typical engineering stress-strain curves obtained from compression tests of the AXM520 alloy and NCs, and (d) compressive properties calculated from 'c'.

ranges from 0.33 to 0.38 for all the NCs. The 'n' values of the NCs gradually increased as the SiC_{np} concentration increased in the NCs. Among the NCs, the NC3.0SiC displayed the maximum 'n' value, i.e., 0.38. Ganguly et al. [81] too reported that the 'n' values increased with the increase in the SiC concentration in the AZ91-Ca-Sb-based nanocomposites. The same trend was also observed for the 'n' values calculated from the compression tests, as shown in Figure 5.2(b). The AXM520 alloy has a 'n' value of 0.30, whereas all the NCs have 'n' values from 0.31 to 0.37.

During plastic deformation, a material undergoes strain-hardening by virtue of its own plastic deformation. In strain-hardening, the stress value of a material is enhanced with the progress of the deformation, i.e., strain. The phenomenon is attributed to the interactions that took place among the dislocations inside the material. The strain-hardening rate (SHR) is related to the true stress (σ) with the true plastic strain (ε) by $\frac{d\sigma}{d\varepsilon}$. Thus, the SHR is the gradient of the true-stress-strain plot in the uniform plastic deformation region. In real life, a material continues to strain-harden until it fractures. However, the geometrical softening overcomes it at the maximum load, i.e., UTS. Beyond the UTS, the geometrical softening dominates over the strain-hardening rate, leading to the material's failure under tension [64]. Figure 5.2(c) shows the variation of SHR against the true plastic strain during the tensile tests for all the materials employed. The SHR decreased linearly with the progress of deformation (i.e., strain) for both the alloy and NCs. Initially, the SHR was higher, and the same declined continuously, leading to the minimum value at the UTS for the plastic strain range considered, as expected. Further, all the NCs exhibited a higher SHR of ~8000-10000 MPa than ~7600 MPa of the AXM520 alloy. The SHR estimated from the compression test for the alloy, and NCs exhibited the same trend, as shown in Figure 5.2(d). A SHR rate of ~7000 MPa was obtained for the AXM520 alloy, whereas all the NCs exhibited relatively higher values of SHR of ~9500 to 10500 MPa. The strain rate, grain size, texture, temperature, twinning, and alloying additions alter the SHR of Mg-based alloys and nanocomposites [64,99-101]. The superior SHR exhibited by the NCs in the current study was probably governed by the potential grain refinement achieved from the nanoparticles and dislocations generated owing to CTE mismatch. A detailed explanation for the improved SHR with a reduction in grain size is available elsewhere [64,98]. Ganguly et al. [81] reported an enhanced SHR following the SiC nanoparticles dispersion in the AZ91-Ca-Sb-based alloy. Lee and Kim [102] too stated a similar observation in the extruded Mg-Carbon-

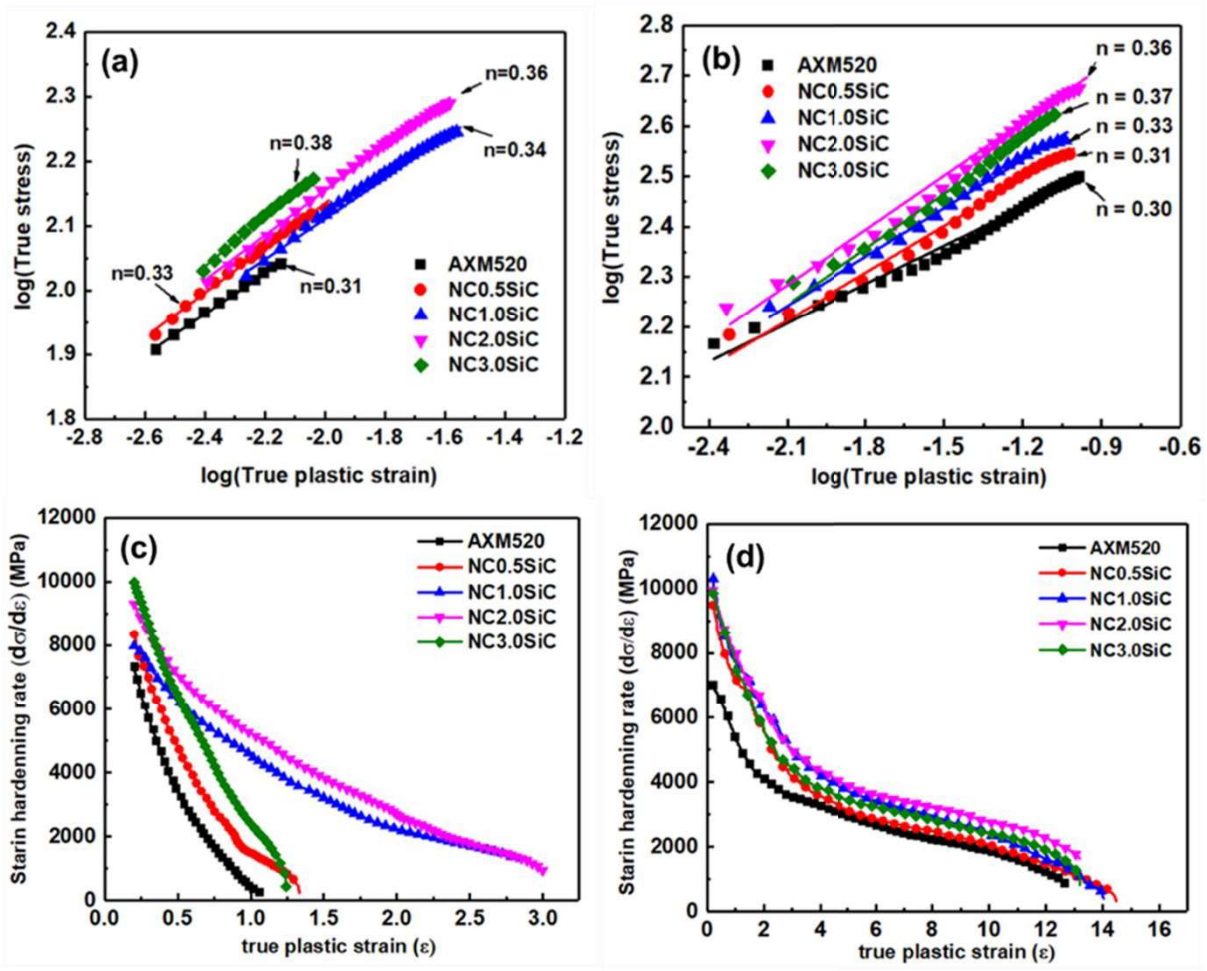

Figure 5.2 Log-log plots of true stress-strain curves for the alloy and NCs displaying the strain hardening exponent (n) calculated from the tensile tests (a) and compression tests (b); variation of strain-hardening rate (dσ/dε) vs. true plastic strain (ε) for the alloy and NCs corresponding to the tensile tests (c), and compression tests (d).

based nanocomposite. A similar strain-hardening response of the extruded Mg-SiC-based composite was observed by Manoharan et al. [103]. Korayem et al. [104] too concluded an increased SHR of pure Mg- and AZ31 alloy-based nanocomposites with the increase of Al_2O_3 nanoparticles content.

5.2 Theoretical prediction of strength and analyses of strengthening mechanisms

The combined effects of strengthening resulting from Hall-Petch, Orowan, CTE mismatch, and load-partitioning contributed to the superior tensile behavior of the AXM520 alloy-based NCs. The grain size of the NCs reduced considerably with an increase in the concentration of the SiC_{np} in the NCs. The contribution to Hall-Petch ($\Delta\sigma_{Hall-Petch}$) strengthening resulting from grain size reduction is predicted as follows [105]:

$$\Delta\sigma_{Hall-Petch} = K{d_m}^{-0.5} \quad \text{Equation 5.2}$$

Here K is a constant related to the material, and d_m is the matrix grain size. In the Orowan mechanism, a dislocation loop is formed around the nanoparticle, resisting the successive dislocation motion and accelerated strain-hardening. In addition, the increased volume fraction of the nanoparticles reduced inter-particle distance between two nanoparticles, restricting dislocation motion further during deformation. The contribution from Orowan strengthening ($\Delta\sigma_{Orowan}$) is estimated as follows [106]:

$$\Delta\sigma_{Orowan} = \frac{0.13G_m b}{\lambda}\ln\frac{d_p}{2b} \quad \text{Equation 5.3}$$

$$\lambda \approx d_p\left[\left(\frac{1}{2V_p}\right)^{\frac{1}{3}} - 1\right] \quad \text{Equation 5.4}$$

where G_m is the modulus in shear of the matrix, b denotes the burger vector, d_p is the diameter of the nanoparticle, λ is the spacing between the nanoparticles, and V_p is the volume fraction of the nanoparticles. The CTE of Mg is significantly different from that of SiC. The dislocation density increased from the difference in CTE values between the AXM520 alloy and SiC_{np}, contributed to the strengthening effect as follows [106]:

$$\Delta\sigma_{CTE} = 1.25G_m b\sqrt{\frac{12\Delta\alpha\Delta T V_p}{bd_p(1-V_p)}} \quad \text{Equation 5.5}$$

where Δα is the difference in CTE values, and ΔT signifies the difference in the processing temperature to the test temperature. The nanoparticles were assumed equiaxed for estimating

the enhancement in YS resulting from the load transfer effect between the matrix alloy and SiC_{np} reinforcement is provided as [106]:

$$\Delta\sigma_l = 0.5V_p\sigma_{o\,[Matrix]} \quad \text{Equation 5.6}$$

The contribution from the individual strengthening mechanism was calculated for all the NCs employing Eq. 5.2 to 5.6, along with the data summarised in Table 5.1. The results obtained are shown in Figure 5.3(a and b). The strengthening from CTE mismatch contributed the most to the overall strengthening of all the NCs. The contributions in strengthening due to the difference in CTE values, Hall-Petch and Orowan increased by 146.0, 18.1, and 121.2 % with the increase in nanoparticle content from 0.5 to 3.0 (wt.%) in the NCs.

Table 5.1 A summary of the parameters used to calculate the strength of the nanocomposites.

Parameters	Value
Hall Petch slope (k_y)	167.2 MPa√μm
CTE (α_{matrix}) of AXM520 alloy	30.40×10^{-6} K^{-1}
CTE (α_{SiC})of SiC_{np}	4.96×10^{-6} K^{-1}
Δα	$\alpha_m - \alpha_{SiC}$
Burgers vector (b)	0.32 nm
Nanoparticle diameter (d_p)	60 nm
Shear modulus (G_m)	17307 MPa
$T_{process}$	250 °C
Volume fraction of nanoparticles V_p	0.0029, 0.0058, 0.0116, and 0.0174

The values of YS of all the NCs were further estimated theoretically employing the 'Summation' [34], 'Modified Clyne' [105], and 'Zhang and Chen' [107] models as stated below, and the results are compared with the experimentally obtained values in Figure 5.3(c).

$$\sigma_{Summation} = \sigma_{0\,[Matrix]} + \Delta\sigma_{Hall-Petch} + \Delta\sigma_{Orowan} + \Delta\sigma_{CTE} + \Delta\sigma_l \quad \text{Equation 5. 7}$$

$$\sigma_{Modified\ Clyne} = \sigma_{0\,[Matrix]} + \sqrt{(\Delta\sigma_{Hall-Petch})^2 + (\Delta\sigma_{Orowan})^2 + (\Delta\sigma_{CTE})^2 + (\Delta\sigma_l)^2} \quad \text{Equation 5. 8}$$

$$\sigma_{Zhang\ and\ Chen} = (1 + 0.5V_p)\left(\sigma_{0\,[Matrix]} + \sigma_{orowan} + \sigma_{CTE} + \frac{\sigma_{orowan} \times \sigma_{CTE}}{\sigma_{0\,[Matrix]}}\right) \quad \text{Equation 5.9}$$

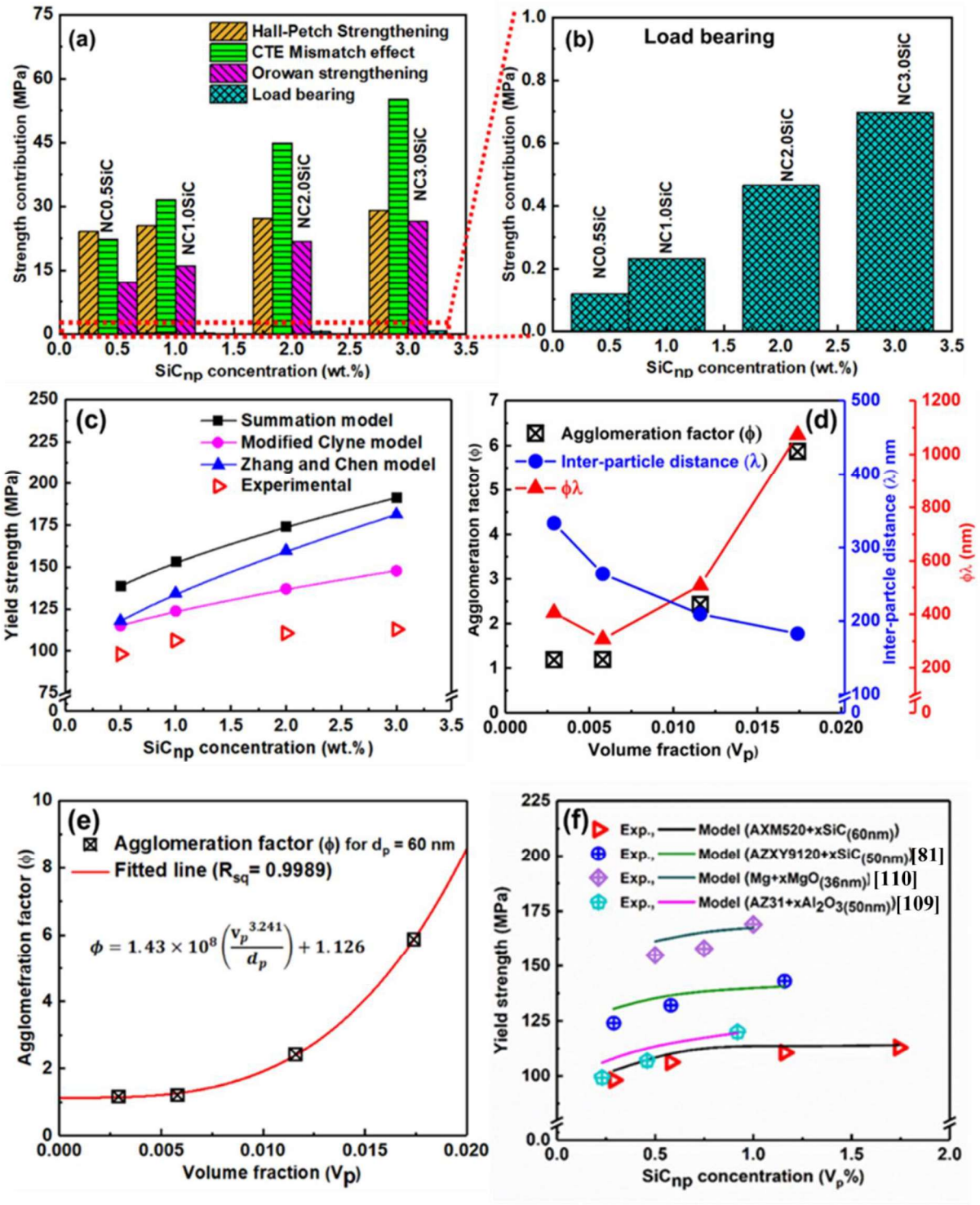

Figure 5.3 (a) Contribution of different strengthening mechanisms to the tensile yield strength (TYS) of the NCs;(b) magnified view of 'a' depicting the load-bearing effect; (c) comparison of the calculated and experimentally determined values of TYS of the NCs; (d) variation of agglomeration factor (φ), inter-particle distance (λ) and 'φλ' with volume fraction (V_p) of the nanoparticles; (e) agglomeration factor (φ) vs. V_p of the nanoparticles with curve fitting; (f) comparison of the experimental and predicted values of TYS.

All the models overestimated the YS of the NCs. The models assumed a homogeneous distribution of nanoparticles. However, the nanoparticles were agglomerated in the NCs during solidification due to their higher surface-to-volume ratio. Thus, the agglomeration of the nanoparticles affected the Orowan strengthening by increasing inter-particle distance (λ). Therefore, an agglomeration factor (ϕ) was introduced in the Orowan equation (Eq. 5.3) to assess the degree of agglomeration in the NCs.

$$\Delta\sigma_{Orowan} = \frac{0.13G_m b}{\phi\lambda}\ln\frac{d_p}{2b} \qquad \text{Equation 5.10}$$

Mallmann et al. [108] reported that the cluster of nanoparticles contributed significantly to $\Delta\sigma_{CTE}$, whereas the contribution from the individual nanoparticle was negligible. They also concluded that the experimental value of $\Delta\sigma_{CTE}$ in the nanocomposite was half of the $\Delta\sigma_{CTE}$ value calculated from Eq. 5.5. Therefore, a value of $0.5\Delta\sigma_{CTE}$ is considered instead of $\Delta\sigma_{CTE}$. Thus, the 'Zhang and Chen' model is modified as follows:

$$\sigma_{Zhang-Chen\,mod} = \left(1 + 0.5V_p\right)\left(\sigma_{o\,[Matrix]} + \frac{\sigma_{Orowan}}{\phi} + \frac{\sigma_{CTE}}{2} + \frac{\sigma_{orowan}\times\sigma_{CTE}}{2\phi\sigma_{o\,[Matrix]}}\right)$$

Equation 5.11

The values of agglomeration factor (ϕ) from Eq. 5.11 and inter-particle distance (λ) from Eq. 5.4 were evaluated for all the NCs, and the same are shown in Figure 5.3(d). The ϕ values remain almost constant up to 0.0058 V_p and then increase sharply, whereas the inter-particle distance (λ) decreases continuously with the increase in V_p, as expected. Thus, the agglomeration of the nanoparticles in the NCs was not significant up to 0.0058 vol. fraction of the SiC_{np} (i.e., NC1.0SiC). Beyond this, the same increases significantly, leading to the highest value in the NC3.0SiC. The parameter $\phi \times \lambda$ indicates the inter-particle distance between two agglomerates, and following an initial decrease, its value gradually increases, as ϕ was dominating over λ. The agglomeration factor (ϕ) is related to the volume fraction (V_p) and average diameter (d_p) of the nanoparticle as follows.

$$\phi \propto \frac{(V_P)^n}{d_P} \qquad \text{Equation 5.12}$$

The exponent n is considered as ϕ increased significantly with the increase in the nanoparticle content. Figure 5.3(e) displays the results of the fitting of Eq. 5.12, and the expression of ϕ is obtained as

$$\phi = \frac{C_1\times(V_p)^n}{d_p} + C_2 \qquad \text{Equation 5.13}$$

where C_1 [=1.430 × 10^8 nm] and C_2 [=1.126] are the fitting constants. The value of n is derived as 3.241. In the present investigation, the average diameter of the nanoparticles, d_p, is 60 nm. The evaluated value of ϕ from Eq. 5.13 was utilized to calculate the YS of all the NCs using the modified Zhang and Chan model proposed in Eq. 5.11. The theoretically calculated YS values of all the NCs are as per the experimental values, as shown in Figure 5.3(f). The equation was also employed to predict the YS of some pure Mg and Mg alloy-based nanocomposites reported in the literature [81,109,110]. The predicted values were pretty close to that of the experimental data, as depicted in Figure 5.3(f).

5.3 Observation of dislocations in post-tensile samples

Figure 5.4 (a to d) shows the dislocation arrangement inside the α-Mg grain of the tensile-tested AXM520 alloy. The TEM bright-field image in Figure 5.4(a) exhibits the dense dislocation forest inside α-Mg grain in the AXM520 alloy. The measured 'd' spacing is approximately 2.49 Å, which corresponds to $[10\bar{1}1]$ '**g**' vector, as shown in Figure 5.4(b). Further, the dark-field images corresponding to '**g**' and '**-g**' vectors are shown in Figure 5.4(c and d). Both images exhibit the **g.b** = 0 invisibility criteria and reveal the dense dislocation forest in the deformed region. The presence of dislocation forest in the grain interior of the primary phase was reported by other researchers as well [111].

The deformed tensile tested samples of the AXM520 alloy and NC2.0SiC were further examined under TEM, and the micrographs are displayed in Figure 5.5(a to d). The TEM BF image and its corresponding two-beam SAED pattern taken from the alloy in Figure 5.5(a and b) reveal the piled-up of numerous dislocations around the C36 phase. The presence of the C36 phase interacted with the dislocations and inhibited their motion, giving rise to the higher dislocation density. Wang et al. too reported an analogous dislocation network around the β-$Mg_{17}Al_{12}$ as well as Al_8Mn_5 phases in the stressed AZ91 and AM50 alloys [112,113]. The BF--TEM image and its corresponding SAED pattern taken from the NC2.0SiC in Figure 5.5(c and d) exhibit that the nanoparticles restricted the dislocation motion as well, and thus there was an additional hindrance to the dislocation motion in the nanocomposites. The consequences of the above factor gave rise to the superior strength of the NCs. Ganguly et al. [81] showed that there was a pile-up of dislocations around the SiC nanoparticles in the AZ91-Ca Sb+2.0SiC_{np} (wt.%) nanocomposite subsequent to the tensile test at 473 K.

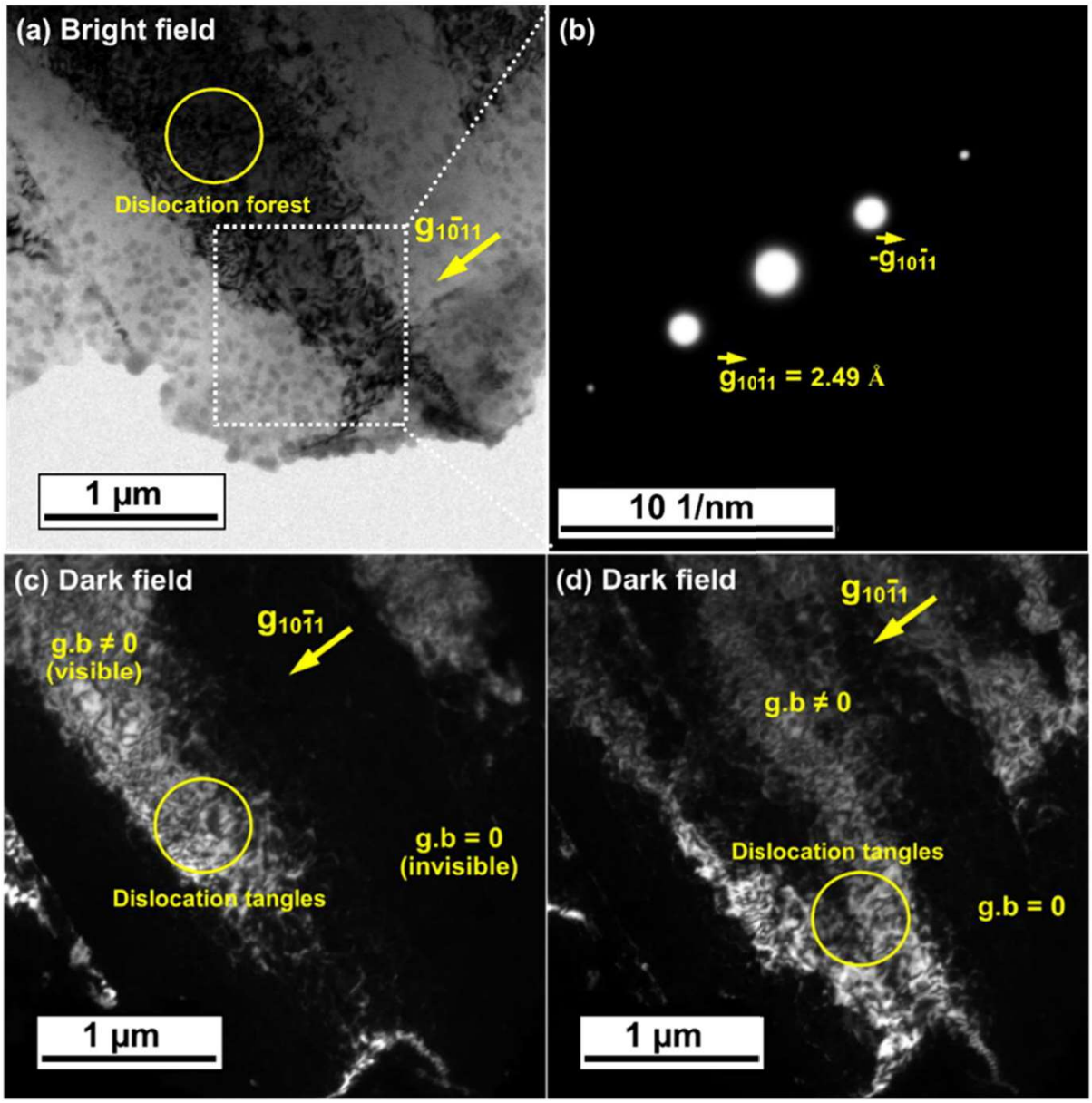

Figure 5.4 (a) TEM bright-field image exhibiting dense dislocation forest inside α-Mg grain in the AXM520 alloy; (b) weak beam diffraction pattern acquired from the region shown in 'a'; (c and d) TEM dark-field images exhibiting dense dislocation tangles [corresponding to spot $\vec{g}_{10\bar{1}1}$ and $-\vec{g}_{10\bar{1}1}$ indicated in 'b', respectively.]

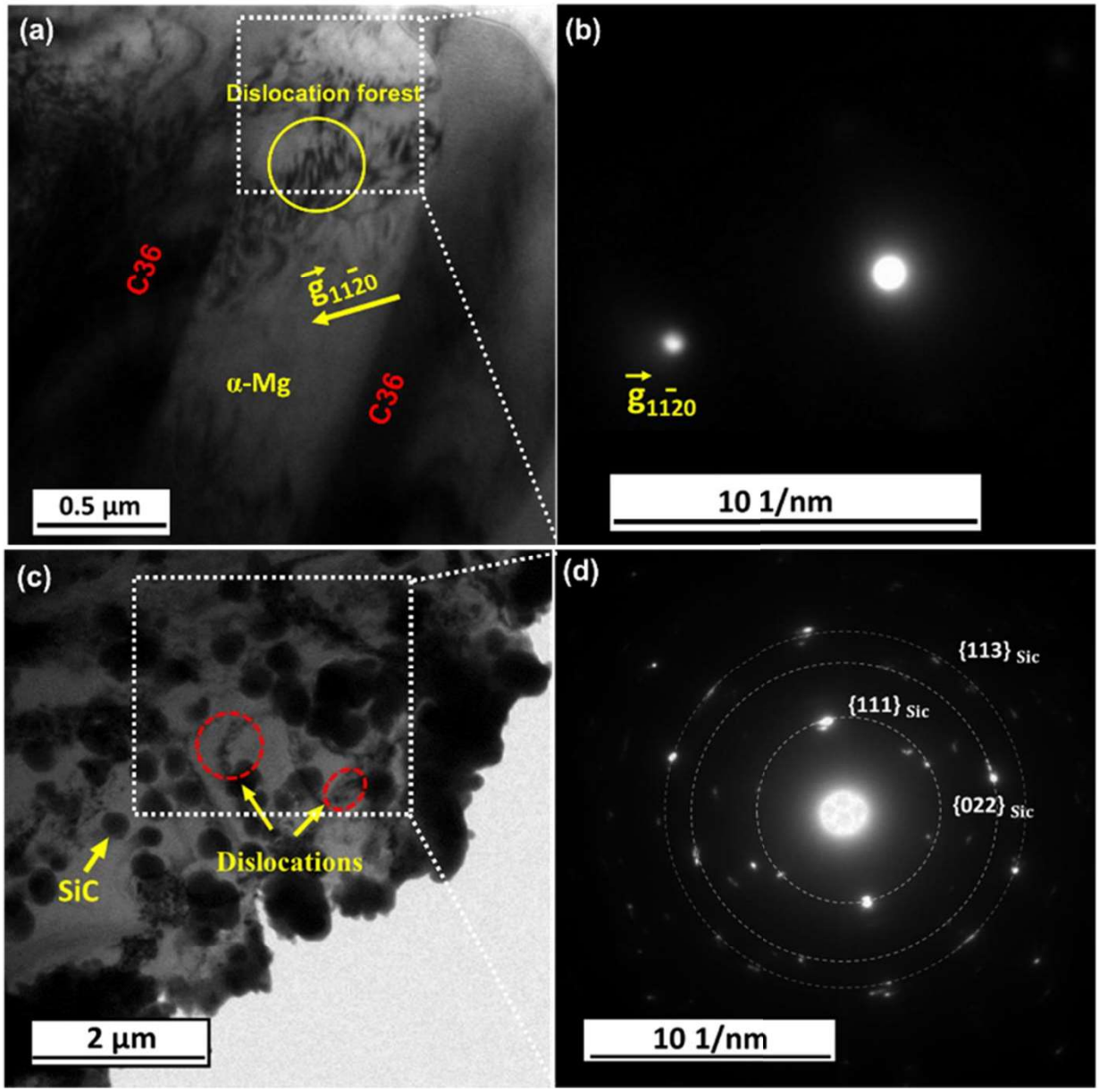

Figure 5.5 (a) TEM BF image exhibiting the dislocation pile-ups at the interface of α-Mg and C36 phases in the AXM520 alloy, and (b) SAED pattern corresponding to 'a' exhibiting two beam condition; (c) interaction of dislocations with the SiC nanoparticles in the NC2.0SiC, and (d) SAED corresponding to 'c'.

5.4 Analyses of fracture surfaces

The SEM images of the tensile fracture surfaces of the AXM520 alloy, NC2.0SiC and NC3.0SiC, are reported in Figure 5.6(a and b). The fracture surface of the AXM520 alloy in Figure 5.6(a) exhibits the presence of a few deep regions (indicated by A) with intergranular cracks. The cracked region (indicated by B) originated at the interface of the α-Mg and C36 phases. The coarse C36 phases acted as a stress raiser and initiated the crack. Subsequently, the crack propagated throughout the interface, leading to failure of the AXM520 alloy by intergranular fracture. The micrograph of the NC2.0SiC in Figure 5.6(b) reveals the presence of multiple cracks (marked by B), cleavage planes (indicated by C), and cleavage steps (indicated by D) indicating a transgranular mode of cleavage fracture [64]. In addition, multiple microvoids (marked as E) were observed in the NC2.0SiC. The presence of feature 'E' suggests that higher energy was absorbed for their formation and coalescence during the tensile deformation of the NC2.0SiC. Thus, it indicates a higher ductility of the NC2.0SiC than that of the unreinforced AXM520 alloy.

Figure 5.6(c and d) presents the fractographs of the compression-tested AXM520 alloy and NC2.0SiC. The fractographs show typical shear bands (marked as A) along the shear direction and shear steps perpendicular to it (marked as B). The presence of microcracks (marked as C) in the shear band regions was also observed. Barnett et al. [114] suggested that the microcracks resulted from the interaction of voids and secondary phases in the AZ31 alloy. The crack propagated through the cross-section of the sample at ∼45 ° with respect to the loading direction. Careful observation of the fracture surface of the AXM520 alloy in Figure 5.6(c) reveals shallow shear steps than the presence of deep shear steps in the NC2.0SiC, as shown in Figure 5.6(d). The higher population of shear bands and wider shear steps indicate higher energy absorption during failure of the NC2.0SiC under compression compared to the alloy and other NCs employed [34,79].

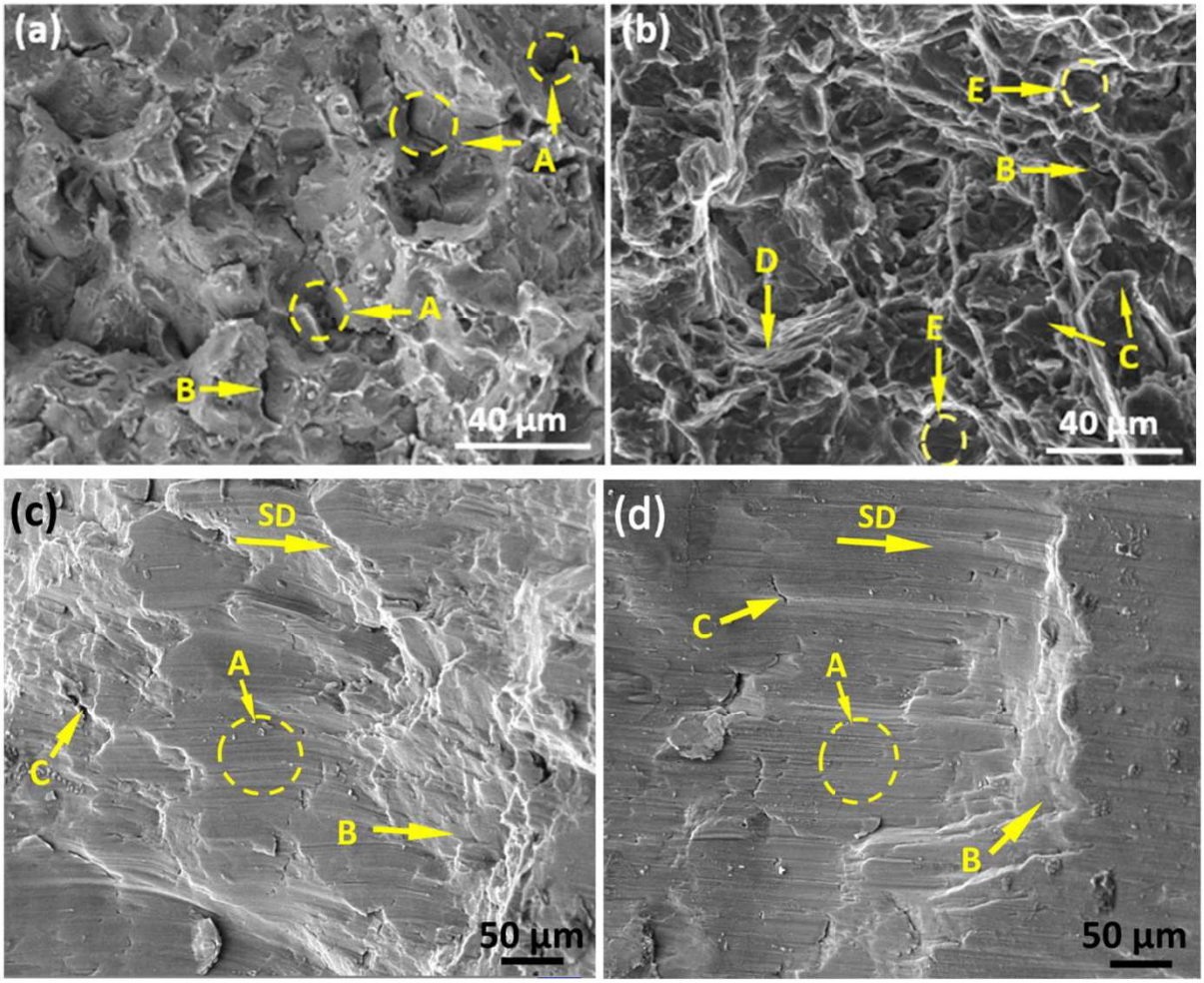

Figure 5.6 Fracture surfaces of the tensile tested (a) AXM520 alloy, and (b) NC2.0SiC; fracture surfaces of the compression tested (c) AXM520 alloy, and (d) NC2.0SiC ('SD' shear direction).

5.5 Summary of chapter 5

In the present chapter, the ambient temperature tensile and compressive properties of the AXM520 alloy and NCs have been evaluated. Detailed analyses of the strain-hardening response and fracture surfaces of the tested specimens are carried out. The major findings from the current chapter are summarized below.

i. All the NCs exhibited superior tensile properties than the AXM520 alloy. The NC2.0SiC with 37.2 and 69.8% enhancement in YS and UTS exhibited the most superior tensile properties. The %El of the AXM520 alloy and NC2.0SiC were 1.03 ± 0.03 and 3.1 ± 0.02%, and it decreased to 1.29 ± 0.02% in the NC3.0SiC. The UTS and %El of the NCs declined with more than 2.0 (wt.%) SiC_{np} to the AXM520 alloy because of the nanoparticle agglomeration.

ii. The superior compressive properties were exhibited by the AXM520 alloy with the SiC_{np} additions. The presence of thicker shear bands in the fractograph of the NC3.0SiC indicated its higher energy absorption capability during failure than the AXM520 alloy.

iii. The strengthening from CTE mismatch contributed the most to the overall strengthening of all the NCs, and the same was 146.0% greater in the NC3.0SiC than the NC0.5SiC. The contribution from Orowan strengthening also increased by 121.2%. However, the Hall-Petch strengthening increased only by 18.1%with the increase in nanoparticle content from 0.5 to 3.0 (wt.%) in the NCs.

iv. The 'Zhang and Chen' model was modified by introducing an agglomeration factor (ϕ). The theoretically predicted YS of all the NCs using the modified 'Zhang and Chen' model matches pretty well with the experimentally obtained values of the NCs.